Meso-FE modelling of textile composites and X-ray tomography

N Naouar, D Vasiukov, C H Park, S V Lomov, P Boisse

J Mater Sci (2020) 55:16969–1698
https://doi.org/10.1007/s10853-020-05225-x

Meso-FE modelling of textile composites and X-ray tomography

N. Naouar[1], D. Vasiukov[2,5], C. H. Park[2,5], S. V. Lomov[3,4], and P. Boisse[1,*]

[1] INSA-Lyon, CNRS, LaMCoS, Univ Lyon, 69621 Lyon, France
[2] Institut Mines-Télécom, Polymers and Composites Technology and Mechanical Engineering Department, IMT Lille Douai, 59508 Douai, France
[3] Department of Materials Engineering, KU Leuven, Leuven, Belgium
[4] Center for Design, Manufacturing and Materials, Skolkovo Institute of Science and Technology, Moscow, Russia
[5] Université de Lille, 59000 Lille, France

ABSTRACT

Among the recent advances made in the analysis and simulation of the mechanical behaviour of composite materials, calculations on a mesoscopic scale make it possible to take into account the internal architecture of a textile and to compute its deformations. The mesoscopic analysis covers the reinforcement behaviour during manufacturing (draping and permeability) and performance in-service (response to applied loads and strains, including damage development). X-ray tomography (μCT) is a tool well suited for determining the 3D internal geometry of the composite. The current characteristics of the μCT devices allow micrometre-scale characterization, providing high-quality geometrical models. The paper presents an overview of μCT-based meso-modelling of textile composites, illustrated by novel modelling results. It covers two segmentation methods (structural tensor and texture analysis), models of the behaviour (deformation response) at meso-scale of textile reinforcements and damage models for textile composites. A set of cases is analysed where X-ray tomography provides the definition of the initial models and the validation of the results obtained by mesoscopic analysis.

Introduction

The analysis and simulation of the behaviour of textiles composite has given rise to a great deal of research in recent decades, most of which is carried out on a macroscopic scale. Nevertheless, some important phenomena occur on a smaller scale both during the processing and when loading the cured composite. Three scales are typically distinguished in the analysis of composite materials or textile

Address correspondence to E-mail: Philippe.Boisse@insa-lyon.fr

https://doi.org/10.1007/s10853-020-05225-x

J Mater Sci (2020) 55:16969–1698
https://doi.org/10.1007/s10853-020-05225-x

composite reinforcements. The macroscopic scale is that of the composite part (Fig. 1a), the mesoscopic scale is that of yarns in the textile (Fig. 1b), and the microscopic scale is that of fibres in the yarn (Fig. 1c).

The three scales are simultaneously present in a textile composite, but mechanical analysis is performed at one of these scales (or at two scales simultaneously) depending on the objectives of the simulation. Currently, industrial composite process simulations and structural analysis are mainly carried out on a macroscopic scale. These simulations concern the forming of textile reinforcements or prepregs (draping) [1], the injection of resin into fibrous reinforcements (LCM, liquid composite moulding) [2–4] or the structural analyses of composite structures [5, 6]. Microscopic scale analysis considers each fibre that is modelled as beams or bars in contact with their neighbours [7–10]. Given a large number of fibres in a yarn (3000 to 48000 in a carbon yarn), microscopic scale analysis is limited to a small domain. Mesoscopic analysis (meso-FE modelling) is at an intermediate scale. The textile composite is seen as a set of yarns in contact with one another. The geometry of each yarn is taken into account. Each yarn is considered as a continuous medium. The mesoscopic analyses concern, on the one hand, the composite reinforcements during preforming (without resin) and, on the other hand, the textile composites with a solid matrix as used in structures. This article deals with these mesoscopic analyses and the use of X-ray tomography to set them up and validate them.

In addition to the nature of the textile composite (dry fabric or consolidated composite), two types of mesoscopic analysis can be distinguished. On the one hand, some recent approaches use a mesoscopic description for a global analysis of the composite part or preform. For example, complete preform drape simulation is based on a mesoscopic modelling [10–15]. This approach provides information at the yarn level and also simulates possible gaps, i.e. separations between yarns. This mesoscopic approach for the entire composite part is undoubtedly promising. As it concerns the entire composite structure, the number of yarns and contacts between yarns is important and the simulation is costly in terms of calculation time, which forces simplified mesoscopic modelling and nevertheless leads to high calculation times. This limits its use at present.

The second type of analysis, which is the most common, consists of mesoscopic analysis that concerns one (or a few) RUC (representative unit cell). The objective is then to determine the mechanical properties of the RUC by submitting it to virtual tests. As the analysis is limited to one or a few unit cells, the model can be very detailed. It is therefore important to have a very precise description of the RUC geometry, orientation and density of the fibres. As will be shown in the following sections, X-ray tomography is a well-adapted tool for this purpose. The boundary conditions depend on the problem under consideration but are often conditions of periodicity [16, 17]. Mesoscopic analysis on an RUC is used to determine the homogenized properties of a textile composite [18–22], to calculate stress and strain in the unit cell [23–25] and to analyse the initiation and propagation of damage [26–30] and failure [31, 32]. In the case of dry textile reinforcements, the mesoscopic analysis of an RUC constitutes virtual

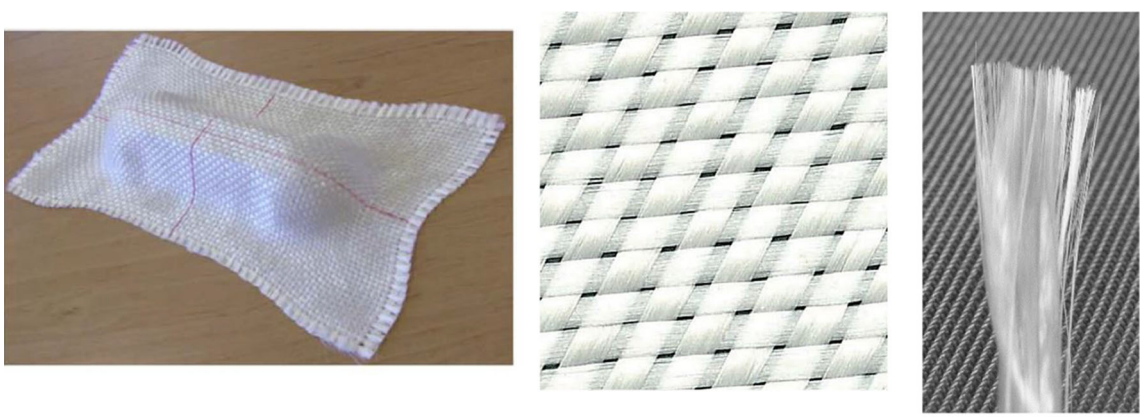

Figure 1 The three scales of a textile composite. **a** Macroscopic, **b** mesoscopic, **c** microscopic.

tests. These make it possible to determine the mechanical properties of the reinforcements for different types of stresses: tension [33, 34], in-plane shear [35, 36], transverse compression [37–42]. The deformed geometry of the RUC (after shear and/or compaction) allows the permeability of the deformed fibrous reinforcement to be calculated by mesoscopic simulation of the resin flow in the reinforcement [43–46].

Tomography can be carried out by absorption mode (this is the mode used by laboratory devices) or by phase contrast or holotomography (in the case of synchrotron sources). Synchrotron sources deliver high flux and can achieve high resolution [47]. In this study on mesoscopic analysis of composite materials, laboratory sources are mainly considered because they have become common and often easily available. They are an accessible tool for mesoscopic analyses. Their characteristics are well suited to the analysis of the three-dimensional geometry of the initial deformed unit cell. Physical quantity measurements from images obtained by X-ray tomography require a segmentation process and image analyses. The segmentation procedure consists in differentiating between various phases in the analysed material. "Image segmentation process" section presents some segmentation methods for composite reinforcements and "Segmentation" section for cured composites. Finite element modelling and simulations are generally carried out to analyse the properties of the material. Some analyses are directly based on the voxels in the image [30, 41, 48]. The spatial resolution of X-ray tomography has increased significantly in previous years. The resolutions of current devices can be less than 100 nm, and the maximum resolution of the majority of devices is close to 1 μm [47]. This resolution becomes less good as the analysed zone moves away from the source. The current spatial resolution of the laboratory devices (a few μm) is well suited for mesoscopic analyses of a composite RUC. The geometry of the yarns and their cross section (width = a few mm) is obtained with accuracy. As will be discussed in the following section, it is possible to acquire the distribution of the fibres (diameter = 7 μm for carbon fibres for example) in yarn sections sufficiently close to the source.

X-ray analysis of effects induced by loadings on materials can be performed in situ. The mechanical test is then performed in the X-ray tomography device [49–51]. Interrupted in situ experiments can be performed when in situ testing is difficult [52, 53]. The tests presented in the present manuscript on composite reinforcements have been interrupted in situ tests. The specimen is analysed by X-ray tomography in its initial state, then loaded outside the tomograph and re-analysed by X-ray tomography in its deformed state. This requires that the creep of the material does not disturb the tests.

For the mesoscopic analysis to be relevant, the finite element model must be accurate both in terms of its geometry and for the direction of the fibres at each point and their density. The purpose of this article is to show that X-ray tomography is a well-suited technique for providing unit cell geometry, orientation and fibre density with the aim of performing a mesoscopic analysis. Another contribution of the X-ray tomography is the possibility of validating the mesoscopic simulations by comparison with X-ray tomography. When the textile composite is subjected to a loading, the deformed geometry, strains, directions and densities of fibres can be measured on the images provided by X-ray tomography and compared to the results of a simulation. This validation is important. The X-ray tomography makes it possible for all the points inside the composite.

The present paper investigates the "road map" for meso-FE analysis of dry textile reinforcements and consolidated textile composites, based on quantified micro-CT images with the resolution in microns range, which is a sufficient precision of the yarn geometry, but not sufficient for recognition of the individual fibres.

Analysis of the geometry by micro-CT

Software for modelling of textile versus X-ray tomography

The mechanical properties of textile reinforcements are highly dependent on their geometry at the mesoscopic scale. Therefore, in order to best predict the mechanical properties of composites, an accurate description of the internal geometry of the fabric is essential. X-ray tomography provides a direct method for determining the internal geometry of textile composite. Two kinds of approaches have been used to construct mesoscopic geometric models of composites for computer simulation:

a. Idealized models can be created by textile software such as WiseTex [54, 55] or TexGen [56].
b. Models obtained by Micro-CT taking into account the details of the geometry of the real textile reinforcement [30, 38, 39, 41, 57–59]. Good resolution of the X-ray tomography leads to accurate geometric models at the mesoscopic scale.

While textile modelling software provides an automatic and robust way to construct geometric depictions of a material for numerical simulations, the models obtained by micro-CT can describe the geometric detail and variability of real textiles, which can be important for accurate numerical simulations.

Image segmentation process

In order to generate a finite element model of the woven fabric, a segmentation is carried out to separate the different yarns, mostly warp and weft yarns. This step presents certain aspects specific to the analysis of woven reinforcements at the mesoscopic scale because it relies on the orientation of the fibres to separate the yarns. Two approaches are quickly presented. The first is suitable for 2D textiles, and the second is necessary for 3D reinforcements. This method calculates the orientation of the fibres at a given point from the components of the structure tensor [60]. The latter is defined by the inner products of the partial spatial derivatives of a greyscale function along the x and y directions in the plane of a 2D reinforcement. The details of the method are given in [57, 60, 61].

Once the orientation of each pixel has been obtained (Fig. 2b), a thresholding in the anisotropy directions of the tows followed by mathematical morphological operations allow to obtain a segmented geometry of the reinforcement without interpenetration (Fig. 2c, d). This method is particularly appropriate in 2D woven reinforcement tomography images in the plan of the fabric. In some situations, segmentation based on structure tensor cannot be used because the stringy yarns aspect is not visible. This is notably the case for 3D reinforcements for images that are perpendicular or that cut the yarns. However, a segmentation method called image texture analysis can be used.

Image segmentation by texture analysis is based on the calculation of grey-level co-occurrence matrices [62]. This method analyses pairs of pixels spatially separated by a given translation. A GLC matrix (grey-level co-occurrence matrix) measures the number of occurrences of pairs of pixel values located at a certain distance in the image. Fourteen parameters were specified [63] so that texture properties can be described with the GLC matrix. The parameters most commonly used are contrast, correlation, energy and homogeneity. The details of the method are given in [39, 62, 63].

A trigger using the most relevant parameter is performed in order to distinguish the warp and weft threads from the segments. The best parameter for yarn segmentation is homogeneity (Fig. 3d). Contrast (Fig. 3a) and energy (Fig. 3c) can be used, but less efficiently. A segmented volume can then be obtained as shown Fig. 4 in the case of a 3D reinforcement.

Mesh generation

From the tomography images, a realistic mesh of the reinforcement is generated. For this purpose, some techniques use the voxel/element method [30, 41, 48, 58]. Each voxel is then considered as a hexahedral element of the mesh. This method is relatively easy to implement but has some disadvantages. One of them is the large number of elements generated. Indeed, the size of the elements (voxel size) depends on the resolution of the image stack. The other difficulty lies in the description of the interface between the tows. The “stepped” representation on the interface is detrimental when analysing the deformation of the dry textile reinforcements, as slippage will occur between the yarns during deformation. An alternative is to mesh the 3D domain of each yarn with finite elements. Both hexahedral and tetrahedral elements were used. However, these two types of elements are not completely satisfactory. Hexahedral elements are well suited to describe the yarn along the fibre direction and are more effective numerically [21, 35, 64]. Nevertheless, the meshing of the cross section of the yarn, usually lenticular or elliptical, with hexahedrons is difficult. In addition, the cross section of the yarn can be effectively meshed by tetrahedrons. However, to obtain accurate results a tetrahedral mesh requires a large number of elements. Prismatic elements allow a compromise between the two aspects [39]. The cross section of the yarn is meshed by triangles that constitute one side of the prism. The quadrangular sides of the prism are

J Mater Sci (2020) 55:16969–1698
https://doi.org/10.1007/s10853-020-05225-x

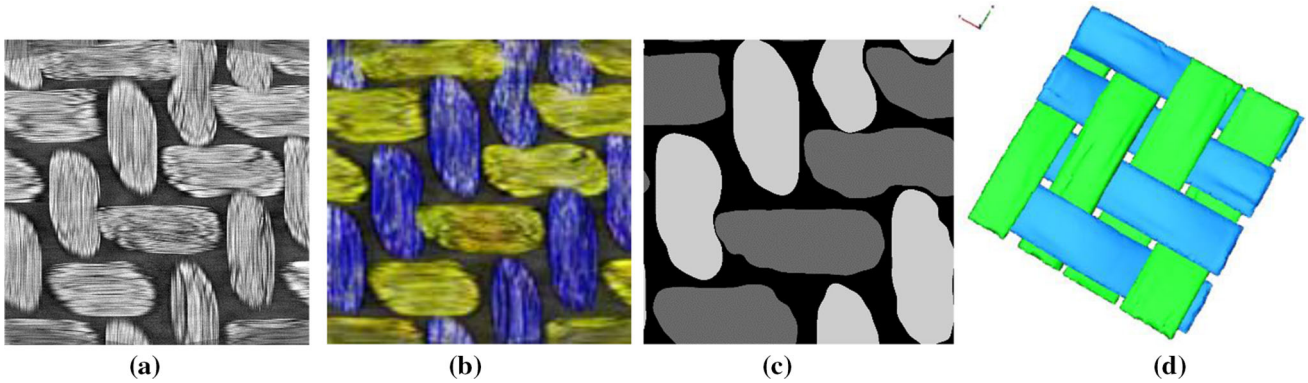

Figure 2 Segmentation of a twill carbon fabric by the tensor structure method. **a** Cut view of the textile reinforcement. **b** Colour orientation map. **c** Thresholding in the anisotropy directions. **d** Segmented geometry without interpenetration.

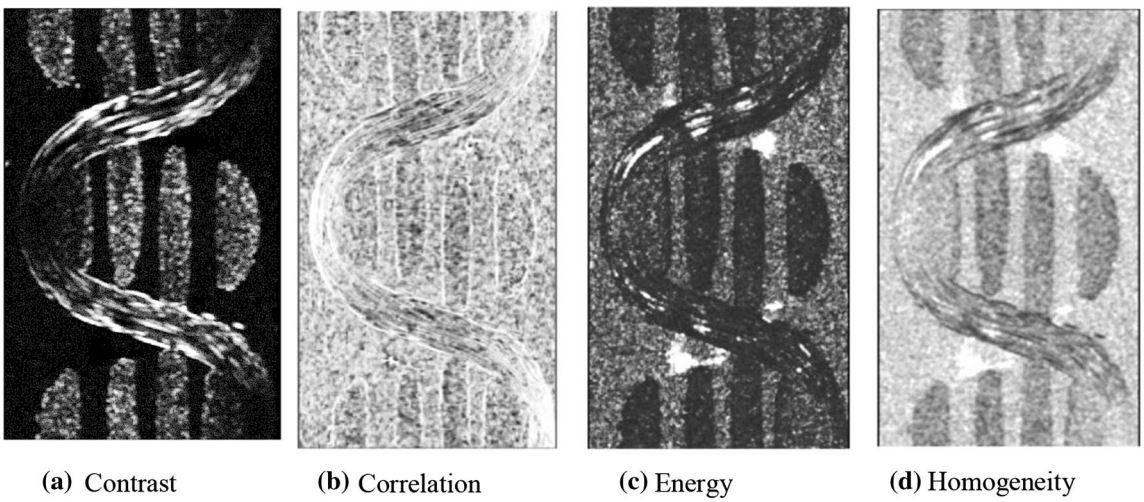

Figure 3 GLCM's statistical parameters applied to 3D reinforcement.

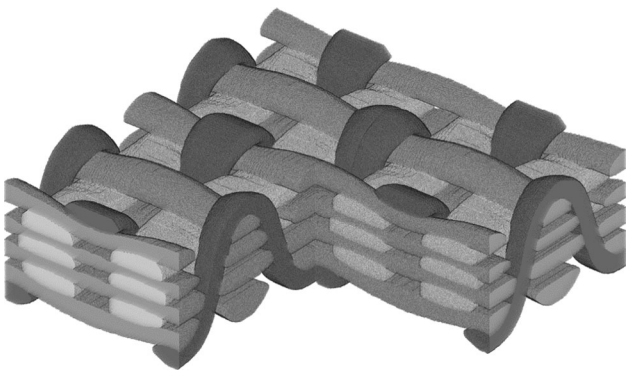

Figure 4 Segmented volume of a 3D fabric.

used in the length of the yarn (Fig. 5a). Thus, these elements have the advantage of adapting to any type of reinforcement morphology while reducing the number of elements compared to tetrahedral elements. The aspect ratio and warping factor of the prism allow to define a quality criterion Q between 0 and 1. The prismatic elements defined here present a criterion between 0.7 and 1 (Fig. 5b).

Meso-scale analyses of textile reinforcements

Mechanical behaviour for meso-scale analysis of dry textiles

On the mesoscopic scale, yarns are considered as continuous solids oriented by a fibre direction. They are in contact with their neighbours, and this directly brings about the behaviour of a woven textile, i.e. high tensile stiffness in the direction of the warp and weft yarns and very low in-plane shear stiffness. The mechanical behaviour of the yarn (considered as a

J Mater Sci (2020) 55:16969–1698
https://doi.org/10.1007/s10853-020-05225-x

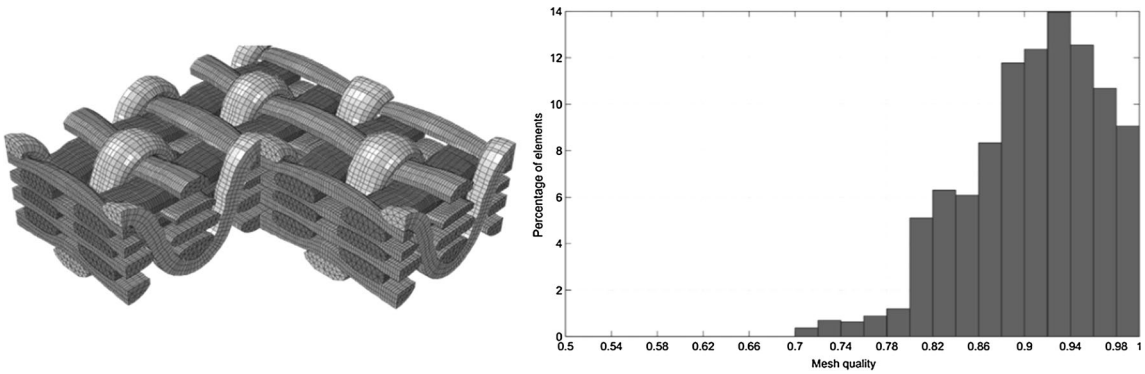

(a) (b)

Figure 5 **a** Mesh of a 3D orthogonal non-crimp fabric; **b** quality of the prismatic elements.

continuous medium) is very specific. The possible slippage between the fibres that constitute the yarn leads to very low shear stiffness. Mechanical behaviour models have to be written in the context of large deformations, because shear strains as well as yarn compactions can be large. Two constitutive models of the mechanical behaviour of the fibre yarn, for use in mesoscopic analysis, are presented below: a hypoelastic model based on the frame of the fibre and a transversely isotropic hyperelastic model. The elastic nature of the mechanical behaviour of yarn can be discussed. Slippage with friction between the fibres provides an irreversible component to this behaviour. However, it has been shown in the case of fibre reinforcement forming that an elastic simulation and a simulation taking into account the irreversibilities give similar results when the loading is monotonous [65]. In this work, only monotonous loadings will be considered.

Hypoelastic model for the fibre yarn

The rate constitutive equations (or hypoelastic equations) constitute an important group of models of mechanical behaviour under large strain [66–68]. These behaviour laws link the objective Cauchy stress rates $\underline{\underline{\boldsymbol{\sigma}}}^{\nabla}$ to the strain rate $\underline{\underline{\mathbf{D}}}$ by the constitutive tensor $\underline{\underline{\underline{\underline{\mathbf{C}}}}}$ and take into account material and geometrical nonlinearities.

$$\underline{\underline{\boldsymbol{\sigma}}}^{\nabla} = \underline{\underline{\underline{\underline{\mathbf{C}}}}} : \underline{\underline{\mathbf{D}}} \tag{1}$$

The objective derivative is a derivative performed in a frame fixed with respect to the material or close enough to the material to be null in the case of rigid body motions. A rotated frame is commonly used for this. The polar decomposition rotation defines the Green Naghdi objective derivative [69] and the corotational frame rotation defines the Jaumann rotation [70]. These two objective derivatives are the most standard and correspond to average rotations of the medium and are adapted to isotropic materials. Jaumann and Green Naghdi's frames do not correspond to the direction of the fibres during the deformation. However, it is important that a frame based on fibre direction be used for an objective integration of stresses when modelling yarn deformation. The following hypoelastic law is based on an orthogonal frame $\underline{f}_i = (\underline{f}_1, \underline{f}_2, \underline{f}_3)$ based on the fibre direction $\underline{f}_1$ (Fig. 6) and whose rotation is that of the fibre at the considered point [71, 72].

From the rate Eq. (1), the stresses are cumulated over each time increment following the scheme of Hughes and Winget [68].

$$\left[\sigma^{n+1}\right]_{f_i^{n+1}} = \left[\sigma^{n}\right]_{f_i^{n}} + \left[\mathbf{C}^{n+1/2}\right]_{f_i^{n+1/2}} \left[\Delta\varepsilon^{n+1}\right]_{f_i^{n+1/2}} \tag{2}$$

The C matrix defines the tangent behaviour in the fibre frame. Image analyses have shown that a hypothesis of transverse isotropic behaviour of the yarn can be made. Longitudinal and cross section strains of the yarn can be distinguished:

$$\begin{aligned}\left[\boldsymbol{\varepsilon}\right]_{f_i} &= \begin{bmatrix} \varepsilon_{11} & \varepsilon_{12} & \varepsilon_{13} \\ & 0 & 0 \\ \text{sym.} & & 0 \end{bmatrix} + \begin{bmatrix} 0 & 0 & 0 \\ & \varepsilon_{22} & \varepsilon_{23} \\ \text{sym.} & & \varepsilon_{33} \end{bmatrix} \\ &= \left[\boldsymbol{\varepsilon}_{\mathrm{L}}\right]_{f_i} + \left[\boldsymbol{\varepsilon}_{T}\right]_{f_i}\end{aligned} \tag{3}$$

The spherical part (change of area) and the deviated part (change of shape) of the deformation in the cross section of the yarn can be separated [35].

J Mater Sci (2020) 55:16969–1698
https://doi.org/10.1007/s10853-020-05225-x

Figure 6 µCT image of a yarn oriented by a fibre direction.

$$[\boldsymbol{\varepsilon}_T]_{f_i} = \begin{bmatrix} \varepsilon_s & 0 \\ 0 & \varepsilon_s \end{bmatrix} + \begin{bmatrix} \varepsilon_d & \varepsilon_{23} \\ \varepsilon_{23} & -\varepsilon_d \end{bmatrix} \tag{4}$$

The transverse behaviour depends on two parameters A and B ($B = C$).

$$\Delta\sigma_s = A\Delta\varepsilon_s \qquad \Delta\sigma_d = B\Delta\varepsilon_d \qquad \Delta\sigma_{23} = C\Delta\varepsilon_{23} \tag{5}$$

The physics of longitudinal behaviour is different depending on whether the yarn is in tension or compression. In tension, the rigidity is high and the parallel fibres lead to a Poisson's ratio of almost zero. In compression, the stiffness is much lower. Longitudinal compression gives rise to large transverse strains (Fig. 7). A Poisson ratio (whose value can be large) is introduced [73]. The matrix of the constitutive tensor in the frame of the fibre takes the following form:

Yarn in tension

$$[C_{tens}]_f = \begin{bmatrix} E_l & 0 & 0 & 0 & 0 & 0 \\ & \frac{A+B}{2} & \frac{A-B}{2} & 0 & 0 & 0 \\ & & \frac{A+B}{2} & 0 & 0 & 0 \\ & & & G_{lt} & 0 & 0 \\ & \text{sym.} & & & B & 0 \\ & & & & & G_{lt} \end{bmatrix}$$

Yarn in longitudinal compression

$$[C_{comp}]_f \begin{bmatrix} E_c & \nu_{ct}A & \nu_{ct}A & 0 & 0 & 0 \\ & \frac{A+B}{2} & \frac{A-B}{2} & 0 & 0 & 0 \\ & & \frac{A+B}{2} & 0 & 0 & 0 \\ & & & G_{lt} & 0 & 0 \\ & \text{sym.} & & & B & 0 \\ & & & & & G_{lt} \end{bmatrix} \tag{6}$$

The components of the constitutive matrix C can be obtained by elementary experimental tests on the yarn or by inverse approaches in the case of tests on the woven reinforcement. In particular, longitudinal compression tests have shown that a Young's modulus E_c in longitudinal compression can be measured and that the corresponding Poisson's ratio can be large (up to 11 for a glass yarn) [73]. This hypoelastic approach will be used in the simulation of RUC deformations in "Consolidated materials" section. In particular, the transverse compaction of a RUC leading to longitudinal compression of binder yarns will be analysed.

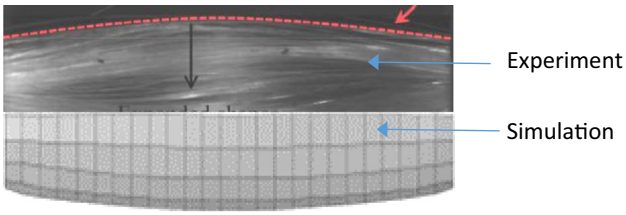

Figure 7 Transverse deformation during a longitudinal compression. Inverse approach to determine the Poisson ratio ($\nu_{ct} = 11$).

Hyperelastic model for the fibre yarn

Hyperelastic models are another possible approach for the mechanical behaviour of yarn fibres. Isotropic models have been first introduced for large deformations of rubber-like materials [74, 75]. Models for anisotropic materials have also been developed for large deformations of certain elastomers and composites [76–78] or biomaterials [79, 80]. The hyperelastic model described below is for fibre yarns assumed to be transversely isotropic. Denoting $\underline{\underline{C}}$ the Cauchy Green deformation tensor, a strain energy potential $w(\underline{\underline{C}})$ gives the second Piola–Kirchhoff stress tensor by derivation:

$$\underline{\underline{S}} = 2\frac{\partial w}{\partial \underline{\underline{C}}} \tag{7}$$

For a transversely isotropic material, the potential is in the form [81]:

$$w = w(I_1, I_2, I_3, I_4, I_5) \tag{8}$$

where $I_1 = \mathrm{Tr}(\underline{\underline{C}})$, $I_2 = \frac{1}{2}\left(\mathrm{Tr}(\underline{\underline{C}})^2 - \mathrm{Tr}(\underline{\underline{C}}^2)\right)$, $I_3 = \det \underline{\underline{C}}$ are the classic invariants of $\underline{\underline{C}}$ and

$$I_4 = \underline{\underline{C}} : (\underline{G}_1 \otimes \underline{G}_1) \quad \text{and} \quad I_5 = \underline{\underline{C}}^2 : (\underline{G}_1 \otimes \underline{G}_1) \tag{9}$$

are invariants obtained from the direction of the fibre $\underline{G}_1$ (Fig. 6). So-called physical invariants are defined

which are directly related to the deformation of the fibre yarn: I_{elong} elongation, I_{comp} compression, I_{dist} distorsion, I_{sh} longitudinal shear. These invariants are functions of the invariants I_1 to I_5 [64]:

$$I_{elong} = \frac{1}{2}\ln(I_4), \quad I_{comp} = \frac{1}{4}\ln\left(\frac{I_3}{I_4}\right), \quad I_{dist} = \frac{1}{2}\ln\left(\frac{I_1 I_4 - I_5}{2\sqrt{I_3 I_4}} + \sqrt{\left(\frac{I_1 I_4 - I_5}{2\sqrt{I_3 I_4}}\right)^2 - 1}\right), \quad I_{sh} = \sqrt{\frac{I_5}{I_4^2} - 1} \tag{10}$$

The potential is assumed to be the sum of potentials depending only on one of the previous invariants:

$$w_{total} = w_{elong}(I_{elong}) + w_{comp}(I_{comp}) + w_{dist}(I_{dist}) + w_{cis}(I_{cis}) \tag{11}$$

Consequently,

$$\underline{\underline{S}}_{total} = 2\left(\frac{\partial w_{elong}}{\partial I_{elong}}\frac{\partial I_{elong}}{\partial \underline{\underline{C}}} + \frac{\partial w_{comp}}{\partial I_{comp}}\frac{\partial I_{comp}}{\partial \underline{\underline{C}}} + \frac{\partial w_{dist}}{\partial I_{dist}}\frac{\partial I_{dist}}{\partial \underline{\underline{C}}} + \frac{\partial w_{cis}}{\partial I_{cis}}\frac{\partial I_{cis}}{\partial \underline{\underline{C}}}\right) \tag{12}$$

The form of the potentials depends on the material. They can be simply quadratic when the behaviour is linear elastic for the considered deformation or more complex (especially for w_{comp}). They are specified for different materials in several studies where this model has been used [15, 64, 82, 83].

X-ray tomography to validate the simulations of mechanical loading on the RUC

As shown in "Analysis of the geometry by micro-CT" and "Mesh generation" sections, X-ray tomography makes it possible to know the geometry of the RUC and to deduce meso-EF models consistent with the real internal geometry of the textile reinforcement. Another interest of X-ray tomography for the meso-EF analyses is to be able to compare the deformation obtained by mesoscopic simulation to the experimental deformation, both inside the RUC and on the edges of the textile reinforcement. An experimental validation for all the points of the elementary cell is important to check the modelling. This experimental deformation can be obtained by in situ tests, i.e. carried out in the tomography set-up, or by interrupted in situ tests where loading is performed outside the tomography set-up and scans are performed in the initial, deformed state.

In the following sections, the hypoelastic model presented in "Hypoelastic model for the fibre yarn" section is used in the FE analyses It is important to take into account the different stiffnesses in tension and longitudinal compression in examples "Compaction of an unbalanced textile reinforcement" and "Compaction of a 3D non-crimp fabric" sections because the binder yarns are in longitudinal compression. Also the high Poisson ratio of the yarns in longitudinal compression is necessary in these simulations.

All the tests presented in the present manuscript have been interrupted in situ tests. The specimen is analysed by X-ray tomography in its initial state, then loaded outside the tomograph (e.g. with the system in Fig. 8 and re-analysed by X-ray tomography in its deformed state. This requires that the creep of the material does not disturb the tests.

Biaxial tensile test

Figure 8 shows a device that can be installed in a tomography set-up for biaxial tensile and in-plane shear loading of a textile cross specimen [84]. The first loading is a biaxial tension (the warp and weft directions are at 90°) on a balanced glass plain weave. Its characteristics are given in Table 1. The tensile strain imposed here is equal in warp and weft directions (equi-biaxial tension). In this case, the yarns are subjected to transverse compaction because of the weaving. For tensile forces of 11 N per yarn, the deformation of a cross section measured by µCT is shown in Fig. 9. The result of a mesoscopic simulation of equi-biaxial tension is in good agreement both for the compaction $h/h0 = 0.89$ and for the yarn boundary [35, 84].

In-plane shear test

An in-plane shear (shear angle = 46°) of the glass plain weave (Table 1) is analysed in Fig. 10. The deformation obtained from the meso-FE simulation is compared to the experimental deformation measured by X-ray tomography [35]. In the deformed state, three sections along the yarn (denoted 1, 2 and 3) are considered and shown in Fig. 10b. For these three sections, the result of the simulation (the contour of the section drawn in continuous black line) is

J Mater Sci (2020) 55:16969–1698
https://doi.org/10.1007/s10853-020-05225-x

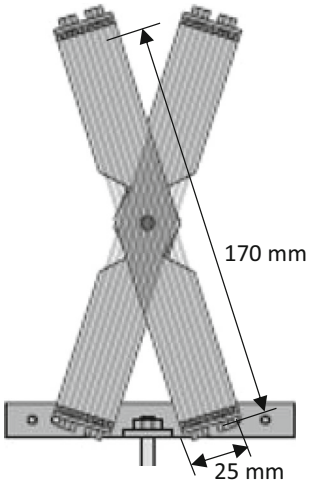

Figure 8 Loading system for imposing biaxial tension or shear loading on a textile cross specimen within the tomography set-up.

compared to the experimental section (in grey) in Fig. 10d. Although there is some difference, the tomographic sections are in good agreement with the sections obtained by simulation. The sections of the sheared textile are clearly different from the initial section. They evolve noticeably along the yarn.

Compaction of an unbalanced textile reinforcement

The glass fabric shown in Fig. 11 is a quasi-unidirectional reinforcement [73]. The warp yarns are the largest. The weft yarns are smaller, and their function is to ensure the cohesion of the fabric. The binder yarns cross the fabric through the thickness. They allow greater permeability in RTM processes. The textile reinforcement is subjected to transverse compaction between two sheets of Plexiglas.

The initial geometry obtained by X-ray tomography and the initial FE mesh of the RUC are shown in Fig. 11. Figure 12 displays a simulation of the transverse compaction where the longitudinal behaviour of the yarn is the same as in tension. In this case, spurious buckling develops for the binder yarn. When the complete behaviours (different in tension and longitudinal compression) [Eq. (6)] are taken into account, the meso-FE simulation is correct and in agreement with the X-ray tomography of the deformed state (Fig. 13). There is no more spurious buckling, and the binder yarn widths are consistent with those measured from μCT.

Compaction of a 3D non-crimp fabric

An orthogonal E-glass 3D orthogonal non-crimp fabric (HYBON 2001®) is presented in Fig. 14 and Table 2. As in the previous section, the loading is a transverse compaction of the fabric reinforcement (compaction strain = 22%). For this analysis, as was the case in "Compaction of an unbalanced textile reinforcement" section, it is important to use a different behaviour when the yarn is in longitudinal tension or compression. Indeed, the Z-yarn is subjected to longitudinal compression in this test. The

Table 1 Glass plain weave

Weaving	Yarn width warp (mm)	Yarn width weft (mm)	Densities warp (yarn/mm)	Densities weft (yarn/mm)	Crimp warp (%)	Crimp weft (%)
Glass plain weave	3.4	3.4	0.25	0.25	0.55	0.55

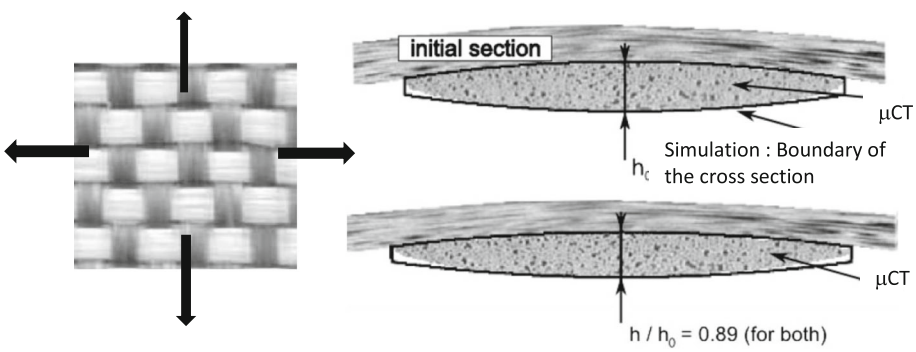

Figure 9 Biaxial tensile test. The experimental cross section obtained by X-ray tomography is in grey. The boundary of the cross section obtained by meso-FE simulation is in a black line.

J Mater Sci (2020) 55:16969–1698
https://doi.org/10.1007/s10853-020-05225-x

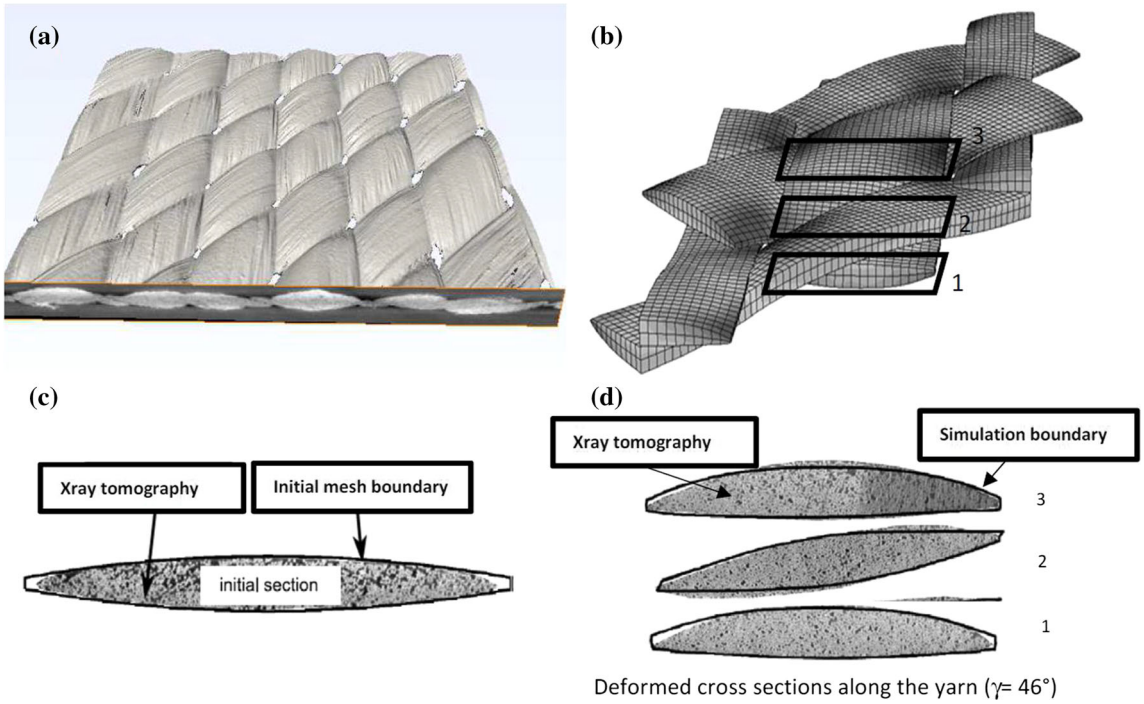

Figure 10 In-plane shear test (46°). Comparison of the deformed shape obtained by tomography (**a**) and meso-FE simulation (**b**). Comparison for the initial cross section (**c**) and for three cross section along the yarn (**d**).

Figure 11 Initial geometry of an unbalanced textile reinforcement and mesh of the RUC.

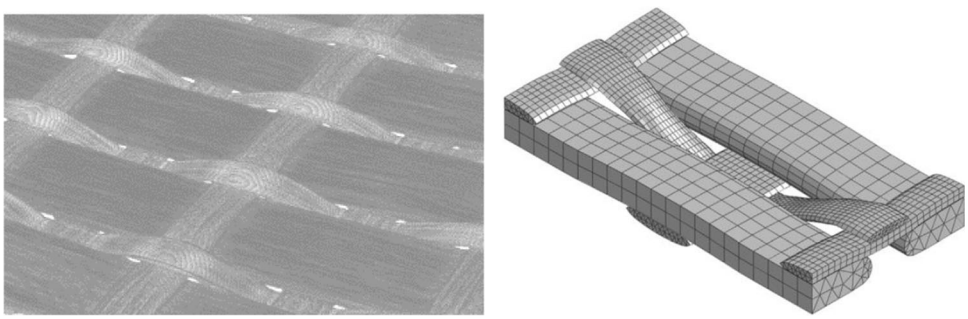

Figure 12 Incorrect simulation of the fabric compaction if the longitudinal compression properties of the binder yarn are the same as in tension.

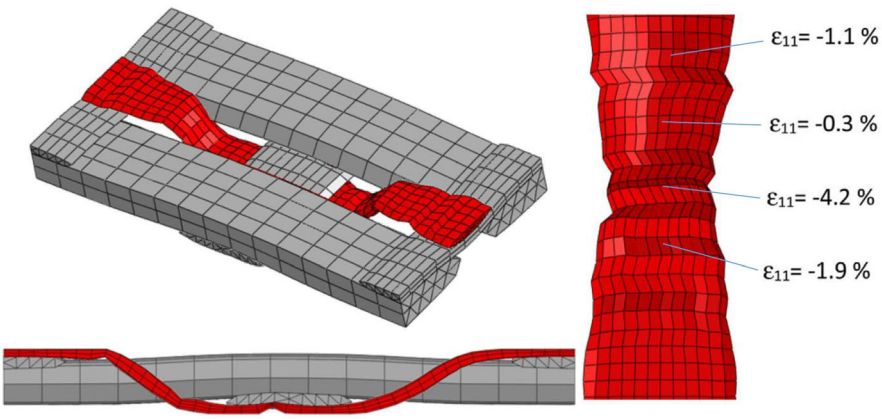

J Mater Sci (2020) 55:16969–1698
https://doi.org/10.1007/s10853-020-05225-x

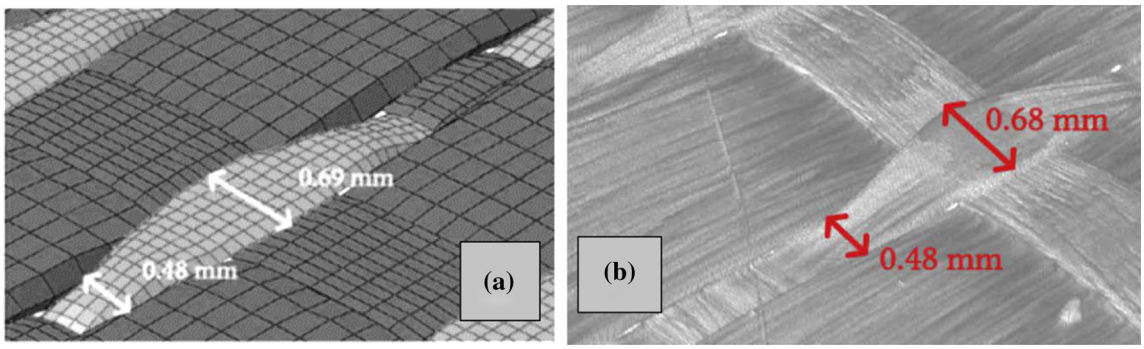

Figure 13 Transverse compaction of an unbalanced fabric. Comparison between (**a**) Meso-FE simulation and (**b**) X-ray tomography.

comparison of the initial geometries and the deformations is shown in Fig. 15. The results are not perfect, but the deformations are in correct agreement (recovery rate = 93%) [39].

It is indeed necessary to ensure that the creep of the material does not disturb the tests. The duration of the scan is about 10 to 20 min. It can be a problem in compaction. But the test is carried out with prescribed displacements. The geometry of the fabric between two plates changes little. The analysis of the influence of creep is certainly an aspect that deserves further investigation.

Consolidated materials

In order to establish a complete methodology of the numerical modelling of textile reinforced composites, in this section we consider three main aspects: image segmentation, material and damage model description.

The main purpose of the material modelling at the meso-scale is to describe behaviour of two or more types of materials. If it comes to textile reinforced composites, the first one is impregnated yarns, described by anisotropic behaviour (anisotropic damage) and the second one is isotropic matrix described as an isotropic material (scalar damage variable). If the issue of manufacturing defects is addressed, then the third phase should be added to represent voids as manufacturing defects.

Segmentation

The structure tensor-based method proposed in [85] is adopted in the present study for impregnated materials. First, the structure tensor is computed at each voxel within a user-chosen neighbouring zone. The structure tensor of a 3D grey-level image I is defined as

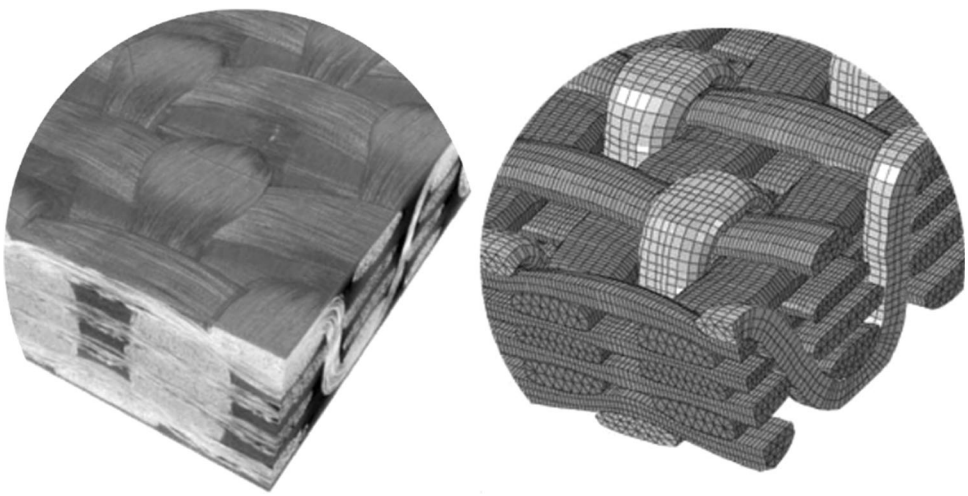

Figure 14 3D orthogonal non-crimp fabric under compaction. X-ray tomography and meso-FE simulation.

J Mater Sci (2020) 55:16969–1698
https://doi.org/10.1007/s10853-020-05225-x

Table 2 E-glass 3D orthogonal non-crimp fabric

Filament diameter (mm)	Number of filament in a yarn	Areal density (g/m^2)	Fabric thickness (mm)	Roving tex (g/km)	Densities warp (yarn/mm)	Densities weft (yarn/mm)	Densities z yarn (yarn/mm)
15	2000	2720	3.1	900	0.47	0.43	0.43

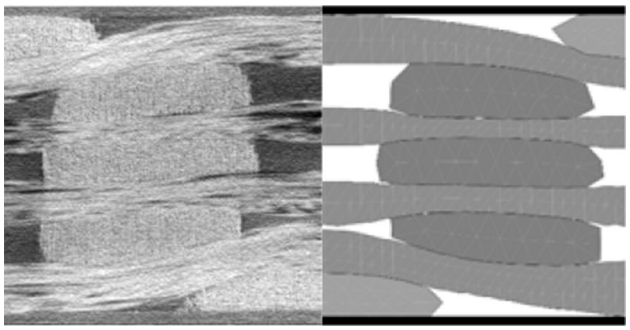

Figure 15 Comparison of the deformed cross section in a compaction (22%) of a 3D fabric.

$$S = \int_W s\mathrm{d}V \quad \text{with} \quad s = \begin{pmatrix} \frac{\partial I}{\partial x}\cdot\frac{\partial I}{\partial x} & \frac{\partial I}{\partial x}\cdot\frac{\partial I}{\partial y} & \frac{\partial I}{\partial x}\cdot\frac{\partial I}{\partial z} \\ \frac{\partial I}{\partial y}\cdot\frac{\partial I}{\partial x} & \frac{\partial I}{\partial y}\cdot\frac{\partial I}{\partial y} & \frac{\partial I}{\partial y}\cdot\frac{\partial I}{\partial z} \\ \frac{\partial I}{\partial z}\cdot\frac{\partial I}{\partial x} & \frac{\partial I}{\partial z}\cdot\frac{\partial I}{\partial y} & \frac{\partial I}{\partial z}\cdot\frac{\partial I}{\partial z} \end{pmatrix} \tag{13}$$

where W stands for the neighbouring window around each voxel. According to [85], the partial differentiation in each direction (X, Y, Z) is performed by a 5-point derivative filter kernel

$D = [1, -8, 0, 8, 1]^{\mathrm{T}}$. The integral is completed by a convolution filter with a uniform kernel whose size is that of the neighbouring zone.

With the structure tensor at hand, various local feature parameters can be deduced for every voxel. The local orientation $\underline{N}$ is expressed by the eigenvector of the structure tensor corresponding to the smallest eigenvalue. The local orientation can be further converted into characteristic angles with different axes according to practical cases. In the present case, weft and interlock yarns are globally parallel to the Y-axis, while warp yarns are globally perpendicular to Y-axis, Thus, the angle ϕ between the orientation $\underline{N}$ and the Y-axis is chosen as the characteristic angle to distinguish the two groups of yarns. A so-called anisotropy degree is defined in Eq. (14) using the eigenvalues of the structure tensor ($\lambda_1 < \lambda_2 < \lambda_3$).

$$\beta = 1 - \frac{\lambda_1}{\lambda_3} \tag{14}$$

Besides, the image grey level is also a very useful local feature to describe the mass density of constituents. To reduce the noise sensitivity, this is averaged within the same neighbouring zone as that used for structure tensor.

$$\mathrm{AVG} = \int_W I(\underline{x})\mathrm{d}V \tag{15}$$

To summarize, three local feature parameters are used in the image segmentation: one is the average grey level AVG, and two others are calculated from the structure tensor (the characteristic angle ϕ and the anisotropy parameter β). They will be further used in a supervised clustering algorithm. One important parameter in this method is the size of the neighbouring zone. A small neighbouring zone retains the local characteristics but makes the result sensitive to image noises, while a large one can reduce noise sensitivity, but the counterpart is to lose local information when averaging within the neighbouring zone.

Gaussian-type supervised clustering is applied to classify the voxels into three groups using the feature parameters presented above. The training sets of each cluster are chosen manually. Each training set I is parameterized by the centroids $\mu^I = [\mu_1, \mu_2, \ldots]^{\mathrm{T}}$ and covariance matrix COV^I of the feature parameters:

$$\begin{cases} \mu^I = \dfrac{1}{n}\sum v^I \\ \mathrm{COV}^I = \left(v - \mu^I\right)\left(v - \mu^I\right)^{\mathrm{T}} \end{cases} \tag{16}$$

where $v^I = [v_1, v_2, \ldots]^{\mathrm{T}}$ is the vector of feature parameters of each voxel in the training set and n is the number of voxels within the training set. These two statistical variables are used for judging which clusters a voxel (outside the training sets) is the most

likely to belong to. In Gaussian-type supervised clustering, the judgment is conducted through a probability value calculated from the Gaussian distribution formula:

$$P^I = \frac{1}{\sqrt{|\mathrm{COV}^I|}} \exp\left[\frac{-1}{2}\left(v-\mu^I\right)^{\mathrm{T}}\left(\mathrm{COV}^I\right)^{-1}\left(v-\mu^I\right)\right] \tag{17}$$

The greatest value of P^I indicates the cluster that the voxel belongs to. The results of this segmentation method are shown in "Material" (Figs. 17 and 18).

Damage models

In this section, we briefly remind the definition of anisotropic behaviour and define the criteria for damage initiation and damage evolution laws. It should be noted that we incorporate into the meso-scale models the information about micro-scale structure at two levels. The first one is yarn properties estimation, if possible by analytical solutions or by numerical homogenization. The second one related to geometry estimation (general shape and orientation) [30, 86–88].

Material modelling is part of continuum damage mechanics, grounded on three basic theorems of equivalent stress, strain and energy. According to the concept of effective Cauchy stress, σ^* acting on fictitious undamaged configuration is related to stress σ in actually damaged configuration via a linear operator M generally called fourth-order damage effect tensor as follows:

$$\sigma^* = M : \sigma \tag{18}$$

where ":" is double contraction. The damage effect tensor is constructed by damage tensor of second order [89]:

$$\mathbf{D} = \Sigma d_i \mathbf{n}_i \otimes \mathbf{n}_i \qquad (i = 1, 2, 3) \tag{19}$$

where $\mathbf{n}_i$ indicates eigenvectors of the damage tensor corresponding to the eigenvalue d_i, which is a scalar that qualified the net area reduction due to the existence of micro-cavities. In an anisotropic damage model for the yarn, the subscript i ranges from 1 to 3, corresponding to the failure modes, such as fibre direction damage and transverse matrix damage along the second and third material principal directions. In this article, the following M tensor in Voigt notation is adopted:

$$M(D) = \mathrm{diag}\Big[(1-d_1)^{-1}; (1-d_2)^{-1}; (1-d_3)^{-1}; (1-d_4)^{-1}; (1-d_5)^{-1}; (1-d_6)^{-1}\Big] \tag{20}$$

where $d_4 = (d_1 + d_2)/2$, $d_5 = (d_1 + d_3)/2$ and $d_6 = (d_1 + d_2)/2$. According to the energy equivalence principle, the damaged complementary energy $\Phi(\sigma, D)$ can be obtained by replacing the Cauchy stress σ by the effective stress σ^* in the undamaged complementary energy, i.e. $\Phi(\sigma^*, 0)$. S^{d} and S^0 represent the compliance tensor of the material in damaged and initially undamaged states, respectively.

$$\frac{1}{2}\sigma : S^{\mathrm{d}} : \sigma = \Phi(\sigma, D) \equiv \Phi(\sigma^*, 0) = \frac{1}{2}\sigma^* : S^0 : \sigma^* \tag{21}$$

After energy identification, it can be proven that $S^{\mathrm{d}} = M^{\mathrm{T}} : S^0 : M$. Correspondingly, the damaged stiffness tensor is obtained as $C^{\mathrm{d}} = \left(S^{\mathrm{d}}\right)^{-1} = M^{-1} : C^0 : \left(M^{\mathrm{T}}\right)^{-1}$ where C^0 denotes the initial stiffness tensor. Combination with Eq. (20), the C^{d} can finally be expressed in Voigt notation as follows:

$$S^{\mathrm{d}} = M^{\mathrm{T}} : S^0 : MC^{\mathrm{d}} = \left(S^{\mathrm{d}}\right)^{-1} = M^{-1} : C^0 : \left(M^{\mathrm{T}}\right)^{-1} C^0 C^{\mathrm{d}}$$

$$C^{\mathrm{d}} = \begin{bmatrix} b_1^2 C_{11} & b_1 b_2 C_{12} & b_1 b_3 C_{13} & 0 & 0 & 0 \\ & b_2^2 C_{22} & b_2 b_3 C_{23} & 0 & 0 & 0 \\ & & b_3^2 C_{33} & 0 & 0 & 0 \\ & & & b_{12} C_{44} & 0 & 0 \\ & \mathrm{sym} & & & b_{13} C_{55} & 0 \\ & & & & & b_{23} C_{66} \end{bmatrix} \tag{22}$$

where $b_i = 1 - d_i (i = 1, 2, 3)$, $b_{jk} = \left(2\left(1-d_j\right)\left(1-d_k\right)/\left(2-d_j-d_k\right)\right)^2 (j, k = 1, 2, 3)$ and C_{mn} (m, n = 1, 2,…, 6) corresponds to the component in the undamaged stiffness matrix.

As for the damage evolution laws for all failure mechanisms (fibre damage, transversal damage and matrix damage), the brittle behaviour is assumed. Regularization based on the crack band model concept [90] directly incorporates the critical strain energy release rate (G_{IC}) as a material parameter to minimize the mesh dependency. Regularization is done on element characteristic length (L). General expression takes an exponential form as follows:

$$d_i = 1 - \frac{1}{f_{di}} \mathrm{e}^{(1-f_{di}) X_I^2 L * / (E_i G_{I,c})} \quad (i = 1, 2, 3;\ I = T(C)L \text{ if } i = 1, \text{ else } I = T(C)T) \tag{23}$$

Another key importance is to select damage initiation criteria which are indicated in Eq. (23). More

https://doi.org/10.1007/s10853-020-05225-x

and detailed information about initiation criteria of all damage mechanisms is described in [30]. However, the damage initiation criterion in the matrix should be recalled. For this purpose, we use hydrostatic pressure-dependent model which is written in the following form:

$$f_{\mathrm{dm}} = \frac{3J_2 + I_1 X_{\mathrm{mt}} X_{\mathrm{mc}}}{X_{\mathrm{mt}} X_{\mathrm{mc}}} \tag{24}$$

where $I_1 = \sigma_{\mathrm{I}} + \sigma_{\mathrm{II}} + \sigma_{\mathrm{III}}$ and $J_2 = \frac{1}{6}\left[(\sigma_{\mathrm{I}} - \sigma_{\mathrm{II}})^2 + (\sigma_{\mathrm{II}} - \sigma_{\mathrm{III}})^2 + (\sigma_{\mathrm{III}} - \sigma_{\mathrm{I}})^2\right]$ are first stress tensor invariant and second invariant of stress deviator expressed in principal stress $\{\sigma_{\mathrm{I}}, \sigma_{\mathrm{II}}, \sigma_{\mathrm{III}}\}$, respectively, $X_{\mathrm{mt}}, X_{\mathrm{mc}}$ are tensile and compressive yield stresses for matrix material, respectively. Plastic deformations are neglected in this work. The matrix was epoxy polymer which behaviour allows to make such a statement.

Assuming the level of approximation and the computational costs, the numerical multi-scale concurrent modelling is still complex. Thus, the well-established analytical approximations are applied here. The elastic properties and strength of yarns in textile composites were estimated from analytical formulations presented in [91].

Material

To highlight the advantages of the proposed simulation strategy we consider an example of warp interlock textile reinforced composite with layer-to-layer binding in which warp yarns are connected by two adjacent layers. X-ray tomography image shows one selected cross section for such types of materials (Fig. 16). These textiles were manufactured at ENSAIT (Roubaix, France), and its areal weight is 0.266 g/cm^2. The yarns are made of E-glass fibres (ρ_{f} = 2.61 g/cm^3, E = 72 GPa and v = 0.22). Textiles were impregnated with epoxy resin (Prime 27) which has the following properties: ρ_{m} = 1.11 g/cm^3, E = 3.3 GPa and v = 0.375. The textiles were impregnated by a rectilinear flow of epoxy resin under the constant inlet pressure of 1 bar in a rectangular mould with the dimensions of 270 × 290 × 2.6 mm^3 using the resin transfer moulding process. For every plate, a systematic measurement of global fibre and void content is adopted with respect to ASTM D2734 standard. The following results are obtained: V_{f} = 0.41 ± 0.012 and V_{v} = 0.038 ± 0.004. Local observations were performed using scanning electron microscopy technique. Three polished cross sections were analyzed for every set of specimens (details can be found in [87]) including at least 30 different yarns of each group (weft/warp). Based on these measurements, local fibre volume fraction (V_{Yf}) and local void fraction (V_{Yv}) were estimated (see Table 3). Finally, all yarn properties calculated according to [91] are presented in Table 3. Through thickness strength (S_{23}) is estimated based on Puck's 3D failure theory for unidirectional composites with taking into account compensated transversal compressive strength (Y_c).

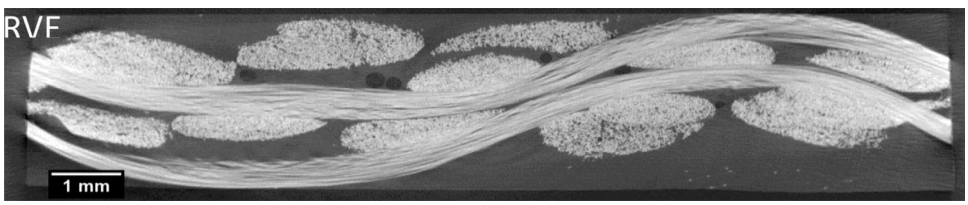

Figure 16 X-ray tomography images of impregnated 3D warp interlocks with manufacturing defects.

Table 3 Elastic and strength properties of yarns with voids

Elastic (in MPa)	E_1	$E_2 = E_3$	$G_{12} = G_{13} = G_{23}$	$v_{12} = v_{13}$(–)	v_{23}(–)
Warp yarns (V_{Yf} = 0.63, V_{Yv} = 0.016)	45835.7	13267.0	4904.6	0.279	0.380
Weft yarns (V_{Yf} = 0.61, V_{Yv} = 0.029)	43896.0	12422.0	4585.7	0.283	0.383
Strength (in MPa)	X_t	X_c	Y_t	Y_c	S_{12}	S_{23}*
Warp yarns (V_{Yf} = 0.63,V_{Yv} = 0.016)	1550	1550	48.4	61.3	24.2	25.1
Weft yarns (V_{Yf} = 0.61,V_{Yv} = 0.029)	1480.7	1480.7	43.4	55.0	21.7	22.7

*Indicates that the component concerns the effective Cauchy stress σ^* (defined in Eq. (18))

Composites samples (dimensions of reconstructed image are 13.71 × 3.14 × 9.99 mm^3) were then analysed using X-ray tomography available in ISIS4D X-ray CT platform (University of Lille, France). The scanning parameters are the following: spot size = 2 μm; voxel size = 8.79 μm; tension = 80 kV; current = 68 μA; frame rate = 10 f/s; scanning time = 20 min. The sample was scanned with 1440 projection images over a 360° rotation. A projection image was the average of six frames to reduce the random noises. Three-dimensional images were reconstructed using the software of RXSolution©.

As can be seen from the image shown in Fig. 16, in addition to geometry reconstruction and local material orientation calculation, we face another key problem, which is manufacturing defects such as voids systematically presented in composite parts manufactured by liquid composite moulding processes.

Analysis of 3D warp interlock segmentation with manufacturing defects

Images were post-processed to deal with beam hardening problems faced during the accusation process. In this section, the structure tensor strategy described in "Segmentation" section is applied. Results of segmentation with different voxel sizes are shown in Fig. 17. The groups of impregnated yarns, whether it is the warp (green colour in Fig. 17a and b) or weft (yellow colour in Fig. 17c and d), are shown along with voids. In all figures, the matrix material is set transparent. It is observed that if the selected size of the final voxel model is smaller (high-resolution images, Fig. 17a, c), then it is possible to capture more details about smaller voids dispersed in the matrix compared with Fig. 17b, d. An important point is that using the structure tensor technique we can segment voids that are located in the matrix only. Voids located inside yarns are much more difficult or almost impossible to segment with the current resolution of the images. Moreover, the main principle of the structure tensor is the usage of the information within a certain integration window, which makes the voids of size close to fibre size simply smeared and overaged within this window.

The key parameter for a correct material model for consolidated composites is local materials orientation which is calculated for every voxel. The final results are shown in Fig. 18. We can see that the local fibre orientation follows properly the yarn geometry.

Comparison of the simulation results with experimental data

Numerical simulation of stress analysis was carried out over the 3D finite element mesh constructed from the segmentation image. The stack of images (see Fig. 16) has been segmented as shown in the previous section (Fig. 17). The course resolution is taken for FE simulations. Segmented images were then directly imported into ABAQUS/Standard as a numerical model in which voxels were represented by C3DR finite elements. The properties of the materials are listed in Table 3. For a case of uniaxial tensile test, loading applied along the warp direction for which the experimental data were obtained from tensile tests. The quasi-static tests were carried out on Instron 1185 test machine with a cross head speed of 2 mm/min. The averaged result from three rectangular (200 × 25 × 2.6 mm^3) tensile specimens with glued composite tabs is shown in Fig. 19a. The width of tensile specimen respects requirement of being at least two times larger than the unit cell size of the textile. Additionally to extensometer, a digital image correlation system VIC2D was used obtaining the following results: Young's modulus in warp direction E_{warp} = 15.31 ± 0.6 (GPa), tensile strength X_{warp} = 225 ± 4 (MPa) and failure strain ε_f = 2.83 ± 0.12 (%).

A comparison between the simulation and experiments is shown in Fig. 19a. Damage initiates at the beginning around ε_i = 0.0025 in both simulation and experimental data, whereas the nonlinear behaviour observed in experiments shows a more pronounced change of slope of the curve at the strain of 0.006. Simulation overestimates the mechanical response in the second part of the stress–strain curve and predicts strength within the error of 5%. Additionally, transversal damages in the warp yarns and matrix cracking are shown in Fig. 19b and c, respectively. Apart from the modification of the elastic and strength properties of the yarn due to the presence of micro-voids inside (Table 3), inter-yarn voids have been included in the matrix. They are seen as white coloured elements in Fig. 19c.

The observed difference between simulations and experiments is caused by the following reasons. The first one is the meso-scale geometry approximation itself which is inevitable. The second reason follows

J Mater Sci (2020) 55:16969–1698
https://doi.org/10.1007/s10853-020-05225-x

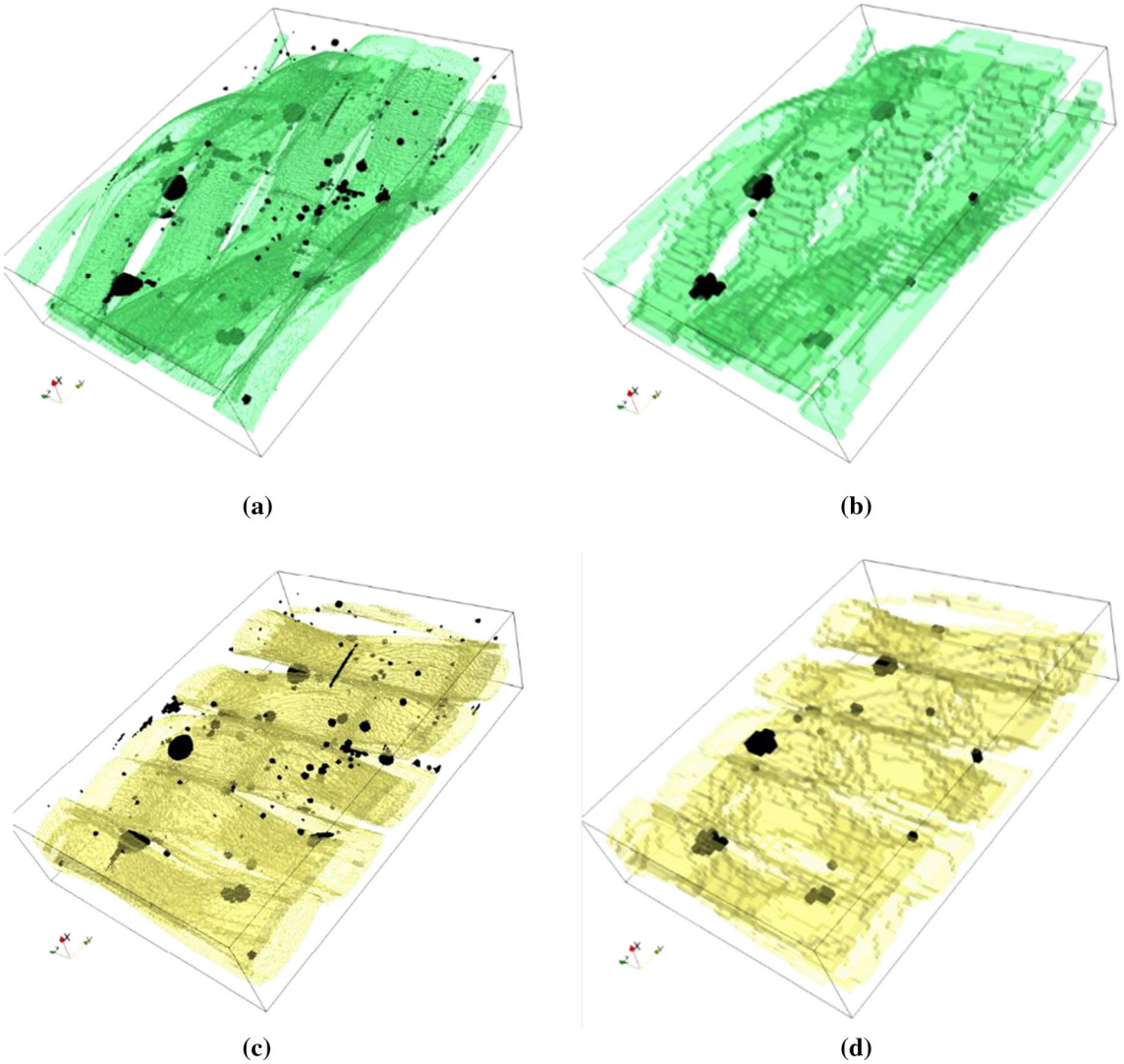

Figure 17 Segmentation using the structure tensor technique of impregnated 3D warp interlock. Comparison between (**a**, **c**) high-resolution warp/weft yarns with voids in the matrix and (**b**, **d**) low-resolution voxel model warp/weft yarns with voids (the matrix is hidden).

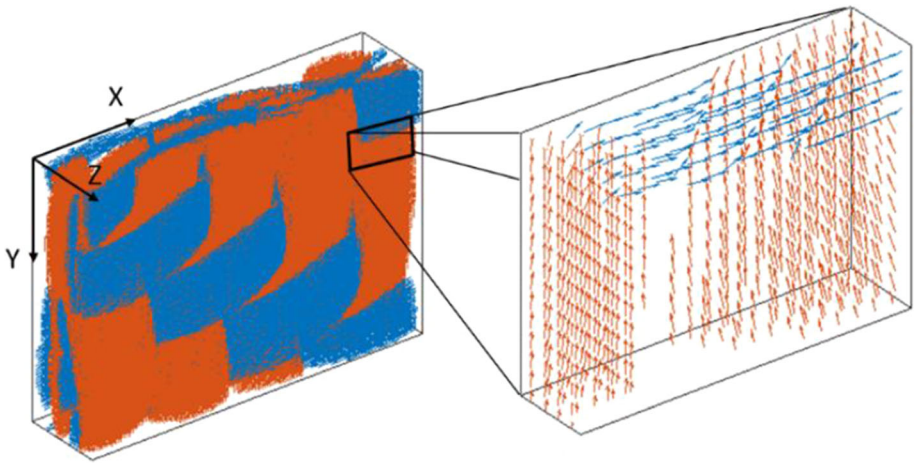

Figure 18 Local fibre orientation of impregnated 3D wrap interlock textile assignment based on the structure tensor technique (all materials are set transparent, and blue and red colours represent warp and weft yarns).

J Mater Sci (2020) 55:16969–1698
https://doi.org/10.1007/s10853-020-05225-x

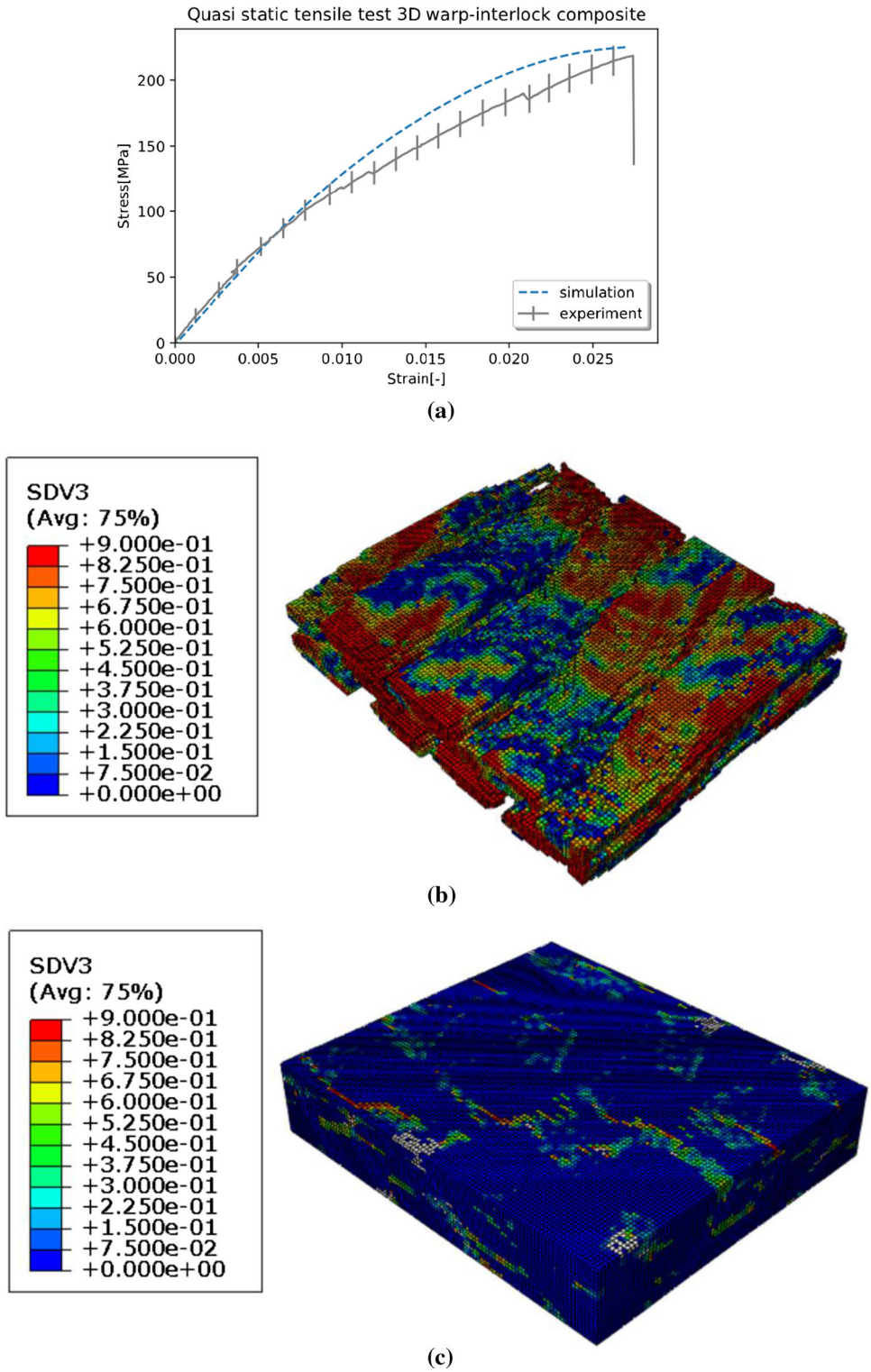

Figure 19 Simulation results: **a** stress–strain curves from simulation and experiments; **b** transversal damage in the yarns and **c** matrix cracking.

from the first one, and the material model did not take into account non-uniform geometry and distribution of the voids inside the yarns. As mentioned in the Introduction section, meso-models incorporating micro-scale information (fibres, matrix and voids) would become a computationally attractive tool for a material design for such complex composites.

Conclusion

The current characteristics of μCT scanners associated with the size of the elementary woven cell of composite materials provide high-quality geometric models for the mesoscopic analysis of textile reinforcements and their composites. The complexity and variability of the geometry is taken into account accurately by models resulting from X-ray tomography. The mesoscopic scale analysis is promising in several areas. It makes it possible to determine by simulation the permeability of a deformed textile reinforcement, to obtain the mechanical characteristics of a composite by homogenization and to analyse its damage. Woven fabric draping simulations based on a mesoscopic model of the complete textile reinforcement are beginning to be used. The influence of the internal geometry is then directly taken into account. In particular, the influence from the manufacturing process on the final mechanical properties of textile composites can be accurately analysed by taking into account the deformation of yarns and voids in a composite part. In spite of those promising advantages, the computing time required by these approaches is still prohibitive.

The objective of this paper was to show that X-ray tomography is a well-suited tool for the mesoscopic analysis of textile reinforcements and consolidated composites. The set of cases presented concerns one (or a few) representative unit cells. Moreover, the latter must be sufficiently close to the source. If the analysis concerns an important part of the composite part or a cell far from the source, the mCT laboratory devices are not suitable. Future developments of these devices will undoubtedly provide solutions to these issues.

Funding

This study was supported by the ANR (French National Research Agency), Grant ANR-18-CE06-0011-04 AMOC. The third and fourth authors acknowledge the European Union (European Regional Development Fund FEDER), the French state and the Hauts-de-France Region council for co-funding the ELSAT 2020 by CISIT project (POPCOM action). The ISIS4D X-ray CT platform has been funded by International Campus on Safety and Intermodality in Transportation (CISIT), the Nord-Pas-de-Calais Region, the European Community and the National Center for Scientific Research. The third and fourth authors also gratefully acknowledge the support of these institutions.

Compliance with ethical standards

Conflict of interest The authors declare that they have no conflict of interest.

References

[1] Gereke T, Döbrich O, Hübner M, Cherif C (2013) Experimental and computational composite textile reinforcement forming: a review. Compos Part A Appl Sci Manuf 46:1–10

[2] Ruiz E, Achim V, Soukane S, Trochu F, Bréard J (2006) Optimization of injection flow rate to minimize micro/-macro-voids formation in resin transfer molded composites. Compos Sci Technol 66(3–4):475–486

[3] Sozer EM, Simacek P, Advani SG (2012) Resin transfer molding (RTM) in polymer matrix composites. In: Advani SG, Hsiao KT (eds) Manufacturing techniques for polymer matrix composites (PMCs). Woodhead Publishing, Singapore, pp 245–309

[4] Bancora SP, Binetruy C, Advani SG, Syerko E, Comas-Cardona S (2018) Effective permeability averaging scheme to address in-plane anisotropy effects in multi-layered preforms. Compos Part A Appl Sci Manuf 113:359–369

[5] Gibson RF (2016) Principles of composite material mechanics. CRC Press, Boca Raton

[6] Jones RM (2014) Mechanics of composite materials. CRC Press, Boca Raton

[7] Miao Y, Zhou E, Wang Y, Cheeseman BA (2008) Mechanics of textile composites: micro geometry. Compos Sci Technol 68(7–8):1671–1678

[8] Durville D (2010) Simulation of the mechanical behaviour of woven fabrics at the scale of fibres. Int J Mater Form 3(2):1241–1251

[9] Latil P, Orgéas L, Geindreau C, Dumont PJ, Du Roscoat SR (2011) Towards the 3D in situ characterisation of deformation micro-mechanisms within a compressed bundle of fibres. Compos Sci Technol 71(4):480–488

[10] El Said B, Ivanov D, Long AC, Hallett SR (2016) Multi-scale modelling of strongly heterogeneous 3D composite structures using spatial Voronoi tessellation. J Mech Phys Solids 88:50–71

[11] Creech G, Pickett AK (2006) Meso-modelling of non-crimp fabric composites for coupled drape and failure analysis.

J Mater Sci 41(20):6725–6736. https://doi.org/10.1007/s10853-006-0213-6

[12] Gatouillat S, Bareggi A, Vidal-Sallé E, Boisse P (2013) Meso modelling for composite preform shaping—simulation of the loss of cohesion of the woven fibre network. Compos Part A Appl Sci Manuf 54:135–144

[13] Bayraktar H, Ehrlich D, Scarat G, McClain M, Timoshchuk N, Redman C (2015) Forming and performance analysis of a 3D-woven composite curved beam using meso-scale FEA. SAMPE J 51(3):23

[14] Thompson AJ, El Said B, Belnoue JP, Hallett SR (2018) Modelling process induced deformations in 0/90 non-crimp fabrics at the meso-scale. Compos Sci Technol 168:104–110

[15] Iwata A, Inoue T, Naouar N, Boisse P, Lomov SV (2019) Coupled meso-macro simulation of woven fabric local deformation during draping. Compos Part A Appl Sci Manuf 118:267–280

[16] Whitcomb JD, Chapman CD, Tang X (2000) Derivation of boundary conditions for micromechanics analyses of plain and satin weave composites. J Compos Mater 34(9):724–747

[17] Tang X, Whitcomb JD (2003) General techniques for exploiting periodicity and symmetries in micromechanics analysis of textile composites. J Compos Mater 37(13):1167–1189

[18] Whitcomb J, Srirengan K, Chapman C (1995) Evaluation of homogenization for global/local stress analysis of textile composites. Compos Struct 31(2):137–149

[19] Carvelli V, Poggi C (2001) A homogenization procedure for the numerical analysis of woven fabric composites. Compos Part A Appl Sci Manuf 32(10):1425–1432

[20] Lomov SV, Bernal E, Ivanov DS, Kondratiev SV, Verpoest I (2005) Homogenisation of a sheared unit cell of textile composites: FEA and approximate inclusion model. Rev Eur Elém 14(6–7):709–728

[21] Obert E, Daghia F, Ladevèze P, Ballere L (2014) Micro and meso modelling of woven composites: transverse cracking kinetics and homogenization. Compos Struct 117:212–221

[22] Rahali Y, Giorgio I, Ganghoffer JF, Dell'Isola F (2015) Homogenization à la Piola produces second gradient continuum models for linear pantographic lattices. Int J Eng Sci 97:148–172

[23] Woo K, Whitcomb JD (2000) A post-processor approach for stress analysis of woven textile composites. Compos Sci Technol 60(5):693–704

[24] Lomov SV, Ivanov DS, Verpoest I, Zako M, Kurashiki T, Nakai H, Hirosawa S (2007) Meso-FE modelling of textile composites: road map, data flow and algorithms. Compos Sci Technol 67(9):1870–1891

[25] Stier B, Simon JW, Reese S (2015) Comparing experimental results to a numerical meso-scale approach for woven fibre reinforced plastics. Compos Struct 122:553–560

[26] Ladevéze P, Lubineau G (2001) On a damage mesomodel for laminates: micro–meso relationships, possibilities and limits. Compos Sci Technol 61(15):2149–2158

[27] Pickett AK, Fouinneteau MRC (2006) Material characterisation and calibration of a meso-mechanical damage model for braid reinforced composites. Compos Part A Appl Sci Manuf 37(2):368–377

[28] Gorbatikh L, Ivanov D, Lomov S, Verpoest I (2007) On modelling of damage evolution in textile composites on meso-level via property degradation approach. Compos Part A Appl Sci Manuf 38(12):2433–2442

[29] Green SD, Matveev MY, Long AC, Ivanov D, Hallett SR (2014) Mechanical modelling of 3D woven composites considering realistic unit cell geometry. Compos Struct 2014(118):284–293

[30] Liu Y, Straumit I, Vasiukov D, Lomov SV, Panier S (2017) Prediction of linear and non-linear behaviour of 3D woven composite using mesoscopic voxel models reconstructed from X-ray micro-tomography. Compos Struct 179:568–579

[31] Tang X, Whitcomb JD (2003) Progressive failure behaviours of 2D woven composites. J Compos Mater 37(14):1239–1259

[32] Ivanov DS, Baudry F, Van Den Broucke B, Lomov SV, Xie H, Verpoest I (2009) Failure analysis of triaxial braided composite. Compos Sci Technol 69(9):1372–1380

[33] Boisse P, Gasser A, Hivet G (2001) Analyses of fabric tensile behaviour: determination of the biaxial tension–strain surfaces and their use in forming simulations. Compos Part A Appl Sci Manuf 32(10):1395–1414

[34] Potluri P, Thammandra VS (2007) Influence of uniaxial and biaxial tension on meso-scale geometry and strain fields in a woven composite. Compos Struct 77(3):405–418

[35] Badel P, Vidal-Sallé E, Maire E, Boisse P (2008) Simulation and tomography analysis of textile composite reinforcement deformation at the mesoscopic scale. Compos Sci Technol 68(12):2433–2440

[36] Chen Q, Boisse P, Park CH, Saouab A, Bréard J (2011) Intra/inter-ply shear behaviors of continuous fiber reinforced thermoplastic composites in thermoforming processes. Compos Struct 93(7):1692–1703

[37] Roux S, Hild F, Viot P, Bernard D (2008) Three-dimensional image correlation from X-ray computed tomography of solid foam. Compos Part A Appl Sci Manuf 39(8):1253–1265

[38] Nguyen QT, Vidal-Sallé E, Boisse P, Park CH, Saouab A, Bréard J, Hivet G (2013) Mesoscopic scale analyses of textile composite reinforcement compaction. Compos Part B Eng 44(1):231–241

[39] Naouar N, Vidal-Salle E, Schneider J, Maire E, Boisse P (2015) 3D composite reinforcement meso FE analyses based on X-ray computed tomography. Compos Struct 132:1094–1104

[40] El Said B, Green S, Hallett SR (2014) Kinematic modelling of 3D woven fabric deformation for structural scale features. Compos Part A Appl Sci Manuf 57:95–107

[41] Wijaya W, Ali MA, Umer R, Khan KA, Kelly PA, Bickerton S (2019) An automatic methodology to CT-scans of 2D woven textile fabrics to structured finite element and voxel meshes. Compos Part A Appl Sci Manuf 125:105561

[42] Wijaya W, Kelly PA, Bickerton S (2020) A novel methodology to construct periodic multi-layer 2D woven unit cells with random nesting configurations directly from μCT-scans. Compos Sci Technol 193:108125

[43] Bickerton S, Šimáček P, Guglielmi SE, Advani SG (1997) Investigation of draping and its effects on the mold filling process during manufacturing of a compound curved composite part. Compos Part A Appl Sci Manuf 28(9–10):801–816

[44] Loix F, Badel P, Orgéas L, Geindreau C, Boisse P (2008) Woven fabric permeability: from textile deformation to fluid flow mesoscale simulations. Compos Sci Technol 68(7–8):1624–1630

[45] Tran T, Comas-Cardona S, Abriak NE, Binetruy C (2010) Unified microporomechanical approach for mechanical behaviour and permeability of misaligned unidirectional fibre reinforcement. Compos Sci Technol 70(9):1410–1418

[46] Zeng X, Endruweit A, Brown LP, Long AC (2015) Numerical prediction of in-plane permeability for multilayer woven fabrics with manufacture-induced deformation. Compos Part A Appl Sci Manuf 77:266–274

[47] Maire E, Withers PJ (2014) Quantitative X-ray tomography. Int Mater Rev 59(1):1–43

[48] Schneider J, Hello G, Aboura Z, Benzeggagh M, Marsal D (2009) A meso-fe voxel model of an interlock woven composite. In: Proceeding of the international conference in composite materials 17th (ICCM17), Edinburgh, Scotland

[49] Buffiere JY, Maire E, Adrien J, Masse JP, Boller E (2010) In situ experiments with X ray tomography: an attractive tool for experimental mechanics. Exp Mech 50(3):289–305

[50] Limodin N, Salvo L, Suéry M, DiMichiel M (2007) In situ investigation by X-ray tomography of the overall and local microstructural changes occurring during partial remelting of an Al-15.8 wt.% Cu alloy. Acta Mater 55(9):3177–3191

[51] McDonald SA, Dedreuil-Monet G, Yao YT, Alderson A, Withers PJ (2011) In situ 3D X-ray microtomography study comparing auxetic and non-auxetic polymeric foams under tension. Phys Status Solidi (b) 248(1):45–51

[52] Salvo L, Cloetens P, Maire E, Zabler S, Blandin JJ, Buffière JY et al (2003) X-ray micro-tomography an attractive characterisation technique in materials science. Nucl Instrum Methods Phys Res Sect B Beam Interact Mater At 200:273–286

[53] Bouttes D, Gouillart E, Boller E, Dalmas D, Vandembroucq D (2014) Fragmentation and limits to dynamical scaling in viscous coarsening: an interrupted in situ x-ray tomographic study. Phys Rev Lett 112(24):245701

[54] Verpoest I, Lomov SV (2005) Virtual textile composites software WiseTex: integration with micro-mechanical, permeability and structural analysis. Compos Sci Technol 65(15–16):2563–2574

[55] Lomov SV, Verpoest I, Cichosz J, Hahn C, Ivanov DS, Verleye B (2014) Meso-level textile composites simulations: open data exchange and scripting. J Compos Mater 48:621–637

[56] Long AC, Brown LP (2011) Modelling the geometry of textile reinforcements for composites: TexGen. In: Boisse P (ed) Composite reinforcements for optimum performance. Woodhead Publishing, Singapore, pp 239–264

[57] Naouar N, Vidal-Sallé E, Schneider J, Maire E, Boisse P (2014) Meso-scale FE analyses of textile composite reinforcement deformation based on X-ray computed tomography. Compos Struct 116:165–176

[58] Straumit I, Vandepitte D, Wevers M, Lomov SV (2017) Identification of the flax fibre modulus based on an impregnated quasi-unidirectional fibre bundle test and X-ray computed tomography. Compos Sci Technol 151:124–130

[59] Krieger H, Seide G, Gries T, Stapleton SE (2018) Geometrical analysis of woven fabric microstructure based on micron-resolution computed tomography data. Appl Compos Mater 25(2):399–413

[60] Bigun J, Bigun T, Nilsson K (2004) Recognition by symmetry derivatives and the generalized structure tensor. IEEE Trans Pattern Anal Mach Intell 26(12):1590–1605

[61] Jeulin D, Moreaud M (2008) Segmentation of 2d and 3d textures from estimates of the local orientation. Image Anal Stereol 27:183–192

[62] Haralick RM, Shanmugam K, Dinstein I (1973) Textural features for image classification. IEEE Trans Syst Man Cybern TSMC 3(6):610–621

[63] Haralick RM, Shapiro LG (1991) In: Haralick RM, Shapiro LG (eds) Computer and robot vision. Addison-Wesley, Boston

[64] Charmetant A, Vidal-Sallé E, Boisse P (2011) Hyperelastic modelling for mesoscopic analyses of composite reinforcements. Compos Sci Technol 71(14):1623–1631

[65] Ghafour TA, Colmars J, Boisse P (2019) The importance of taking into account behaviour irreversibilities when

simulating the forming of textile composite reinforcements. Compos Part A Appl Sci Manuf 127:105641

[66] Truesdell C (1955) Hypo-elasticity. J Ration Mech Anal 4:83–133

[67] Xiao H, Bruhns OT, Meyers A (1998) On objective corotational rates and their defining spin tensors. Int J Solids Struct 35(30):4001–4014

[68] Hughes TJ, Winget J (1980) Finite rotation effects in numerical integration of rate constitutive equations arising in large-deformation analysis. Int J Numer Methods Eng 15(12):1862–1867

[69] Dienes JK (1979) On the analysis of rotation and stress rate in deforming bodies. Acta Mech 32(4):217–232

[70] Dafalias YF (1983) Corotational rates for kinematic hardening at large plastic deformations. Trans ASME J Appl Mech 50:561–565

[71] Boisse P, Gasser A, Hagege B, Billoet JL (2005) Analysis of the mechanical behaviour of woven fibrous material using virtual tests at the unit cell level. J Mater Sci 40(22):5955–5962. https://doi.org/10.1007/s10853-005-5069-7

[72] Boisse P, Hamila N, Helenon F, Hagège B, Cao J (2008) Different approaches for woven composite reinforcement forming simulation. Int J Mater Form 1(1):21–29

[73] Wang D, Naouar N, Vidal-Salle E, Boisse P (2018) Longitudinal compression and Poisson ratio of fibre yarns in mesoscale finite element modelling of composite reinforcements. Compos Part B Eng 141:9–19

[74] Rivlin RS, Saunders DW (1951) Large elastic deformations of isotropic materials VII. Experiments on the deformation of rubber. Philos Trans R Soc Lond Ser A Math Phys Sci 243(865):251–288

[75] Ogden RW (1997) Non-linear elastic deformations. Courier Corporation, Chelmsford

[76] Dörr D, Joppich T, Kugele D, Henning F, Kärger L (2019) A coupled thermomechanical approach for finite element forming simulation of continuously fiber-reinforced semi-crystalline thermoplastics. Compos Part A Appl Sci Manuf 125:105508

[77] Guo Z, Peng X, Moran B (2007) Large deformation response of a hyperelastic fibre reinforced composite: theoretical model and numerical validation. Compos Part A Appl Sci Manuf 38(8):1842–1851

[78] Agoras M, Lopez-Pamies O, Castañeda PP (2009) A general hyperelastic model for incompressible fibre-reinforced elastomers. J Mech Phys Solids 57(2):268–286

[79] Weiss JA, Maker BN, Govindjee S (1996) Finite element implementation of incompressible, transversely isotropic hyperelasticity. Comput Methods Appl Mech Eng 135(1–2):107–128

[80] Holzapfel GA, Gasser TC, Ogden RW (2000) A new constitutive framework for arterial wall mechanics and a comparative study of material models. J Elast Phys Sci Solids 61(1–3):1–48

[81] Boehler JP (1987) In: Boehler JP (ed) Applications of tensor functions in solid mechanics, vol 292. Springer, New York

[82] d'Agostino MV, Giorgio I, Greco L, Madeo A, Boisse P (2015) Continuum and discrete models for structures including (quasi-) inextensible elasticae with a view to the design and modelling of composite reinforcements. Int J Solids Struct 59:1–17

[83] Ghazimoradi M, Naouar N, Carvelli V, Boisse P (2019) Numerical modelling of the mechanical behaviour of tetraxial technical textiles. J Mater Sci 54(4):3632–3647. https://doi.org/10.1007/s10853-018-3084-8

[84] Badel P (2008) Ph D thesis, University of Lyon

[85] Straumit I, Lomov SV, Wevers M (2015) Quantification of the internal structure and automatic generation of voxel models of textile composites from X-ray computed tomography data. Compos Part A Appl Sci Manuf 69:150–158

[86] Vasiukov D, Panier S, Hachemi A (2015) Non-linear material modelling of fibre-reinforced polymers based on coupled viscoelasticity–viscoplasticity with anisotropic continuous damage mechanics. Compos Struct 132:527–535

[87] Chen Y, Vasiukov D, Park CH (2018) Influence of voids presence on mechanical properties of 3D textile composites. IOP Conf Ser Mater Sci Eng 406(1):012006

[88] Chen Y, Vasiukov D, Gélébart L, Park CH (2018) Fast Fourier transform solver for damage modelling of composite materials. JMST Adv 1(1–2):49–55

[89] Murakami S (1983) Notion of continuum damage mechanics and its application to anisotropic creep damage theory. J Eng Mater Technol 105:99–105

[90] Bazant Z, Oh B (1983) Crack band theory of concrete. Mater Struct 1983(16):155–177

[91] Chamis CC, Abdi F, Garg M, Minnetyan L, Baid H, Huang D, Housner J, Talagani F (2013) Micromechanics-based progressive failure analysis prediction for WWFE-III composite coupon test cases. J Compos Mater 47(20–21):2695–2712